Macalester Journal of Physics and Astronomy

Volume 8
Issue 1 *Spring 2020*

Article 17

May 2020

Calculating centrality variables and geometric quantities associated with high energy Pb+Pb and Au+Au collisions using a Monte Carlo Glauber model

Anya Wolterman
Macalester College, awolterm@macalester.edu

Calculating centrality variables and geometric quantities associated with high energy Pb+Pb and Au+Au collisions using a Monte Carlo Glauber model

Abstract

The Glauber model provides insight into the initial state of nuclear collisions by treating them in terms of the interactions between their constituent nucleons, in accordance with theories about the scattering of composite particles. These phenomenological techniques are commonly used to determine various geometric quantities associated with such complex, femtoscopic many-body systems. The Monte Carlo Glauber approach uses a random impact parameter and measured nuclear densities to investigate quantifiable properties like particle multiplicity and average geometric eccentricity for heavy ion collisions. The former involves incorporating a particle production model to plot the total transverse energy or the number of particles produced at mid-rapidity, both being measures of centrality. The latter delves into the eccentricity of different event classes, which can be used to characterize various collision shapes for measurements of elliptic flow of heavy mesons. The results of both applications are then compared with analyses from CMS and STAR as part of efforts to study the properties of the ultra-hot, super-dense phase of matter known as the Quark-Gluon Plasma.

Calculating centrality variables and geometric quantities associated with high energy Pb+Pb and Au+Au collisions using a Monte Carlo Glauber model

Anya Wolterman[1], Advisor: Professor Manuel Calderón de la Barca Sánchez[2]
[1] Department of Physics and Astronomy, Macalester College, 1600 Grand Ave, St Paul, MN 55105
[2] Department of Physics, University of California - Davis, 1 Shields Ave, Davis, CA 95616

1 Introduction

High energy physics seeks to further our understanding of the fundamental nature of matter, from the familiar world of electromagnetically-interacting electrons and nucleons to a more exotic phase of matter thought to have existed only microseconds after the Big Bang. One of these highly sought after and studied states is known as the Quark-Gluon Plasma (QGP), in which baryonic matter exists as a hot, dense mixture of quarks and gluons, collectively known as partons. The partons are believed to have occupied this color-deconfined state within the first 10^{-6} to 10^{-5} seconds of the universe's existence, when the temperature was still above 10^{12} K. This transpired just prior to the partons undergoing a phase transition in which the strong force bound them together and they coalesced into more familiar hadronic matter.

In order to recreate the extreme pressure and temperature conditions of this early environment, particle colliders like the LHC and RHIC accelerate heavy atomic nuclei to ultra-relativistic speeds in order to reach the highest possible energies in the smallest possible volumes [1]. The resulting violent collisions effectively melt the nucleons, transforming the confined quarks that had been held within hadrons due a property of the strong force known as asymptotic freedom into a quasi-free QGP state. On the order of 10^{-23} seconds later, the quarks, anti-quarks, and gluons created from the available energy recombine into hundreds of hadrons that explode outward into the surrounding detectors. Phenomenological techniques known as Glauber models are used to estimate various immeasurable quantities associated with such events, including the offset between the nuclei and the number of nucleons that interact, based on experimentally measured energies and particle yields. Through this type of computer modelling, complex heavy ion collisions are simplified into sequences of individual nucleon-nucleon interactions consistent with the scattering of composite particles. Calculations of additional geometric quantities, like the eccentricity, can provide insights into the behavior of the quarks and gluons as they flow out of the central interaction region. These analyses all fit into the broader scientific investigation of the ultrahot, super-dense phase of matter referred to as the QGP.

1.1 Quantum Chromodynamics

Understanding the bulk and transport properties of the QGP and the phase transition to this color-deconfined state first requires a better comprehension of the theory regarding the fundamental force governing such a system: quantum chromodynamics (QCD). Protons and neutrons are each composed of three valence quarks, confined within each nucleon by the strong nuclear force, an interaction described by QCD. It is one of the three quantum field theories that make up the Standard Model of all fundamental interactions among elementary particles; the other two are quantum electrodynamics (QED) for the electromagnetic force, and quantum flavordynamics (QFD) for the weak nuclear force. Interestingly, most of the baryonic mass in the universe actually comes from quantum chromodynamics. The Higgs mechanism is responsible for the mass of the quarks

themselves, but that is only 1% of the total nucleon mass, meaning the remaining 99% comes from the strong interactions between the quarks [2]. Furthermore, nucleons comprise most of the mass of the atom and thus QCD is responsible for the majority of everyday mass. Hence, understanding the behavior of this force at high energies by studying the QGP could contribute to a better understanding of nuclear matter in general.

The strong force is mediated by eight neutral gluons, which are massless bosons (i.e. they carry whole-number spin) that are self-interacting because they can carry color and anti-color charge. Color charge is analogous to electric charge, except for the fact that it is not static; quarks can change color because the gluons they exchange carry color charge themselves, while an electron will always be negatively-charged since the QED mediator, the photon, carries no electric charge. There are three color charges—red, green, blue—and their respective anticolors—anti-red, anti-green, anti-blue—with neutral "white" combinations being made as either color plus anticolor (with these quark pairs being called mesons) or as three different colors or anticolors (with triplets being known as baryons).

One of the most unusual aspects of QCD is the phenomenon of asymptotic freedom, a product of gluon self-coupling in which the strong force increases as the distance between the color-charged objects grows; in other words, the coupling strength gets weaker as the quarks get closer together, thereby making it seem like the quarks are free at small distances. This is entirely contrary to the familiar behavior of the electromagnetic and gravitational forces, which drop off in strength as the distance between the interacting objects increases. High energies, and therefore short distances, are sought out since the coupling constant shrinks in this limit. This bizarre property, which requires a non-Abelian gauge theory to be described, complicates the study of QCD-interacting matter like the Quark-Gluon Plasma [3].

1.2 Quark-Gluon Plasma

In the first few microseconds of the universe (the "primordial universe" shown in Fig. 1), the quarks and gluons that make up the hadrons in ordinary nuclear matter existed as this strongly-interacting yet deconfined QGP phase. The high temperatures and densities allow the partons to be asymptotically free. Given the timescale of its proposed existence, studying the QGP provides insights into the properties of the very early universe, in addition to being a medium through which quantum chromodynamics can be studied (since the strong force governs the behavior of the QGP). One of the key difficulties that arises when trying to study the QGP is the previously mentioned phenomenon of confinement due to asymptotic freedom. As one tries to separate the quarks, the system reaches a point where it becomes energetically favorable to create a new quark-antiquark pair out of the vacuum, which can then recombine with the escaping quark to make a new hadron. Given that behavior, free solitary quarks have never been observed, and the closest that has been achieved is this quasi-free QGP state.

The QGP is called a "plasma" because it was expected to behave like an ultrahot weakly-coupled gas of charged particles. However, experiments have found a state of matter that acts more like a strongly-coupled liquid—a perfect fluid exhibiting collective flow with almost no viscosity. The best parameter to describe the observed system is one typically used for liquids: the ratio of shear viscosity to entropy density, η/s. This quantity was found to be nearly zero, making this substance one of the first experimentally accessible perfect liquids ever isolated in a lab but also suggesting that a true quark-gluon "plasma" may not have formed or that the models of the very early universe may be in need of revising [4].

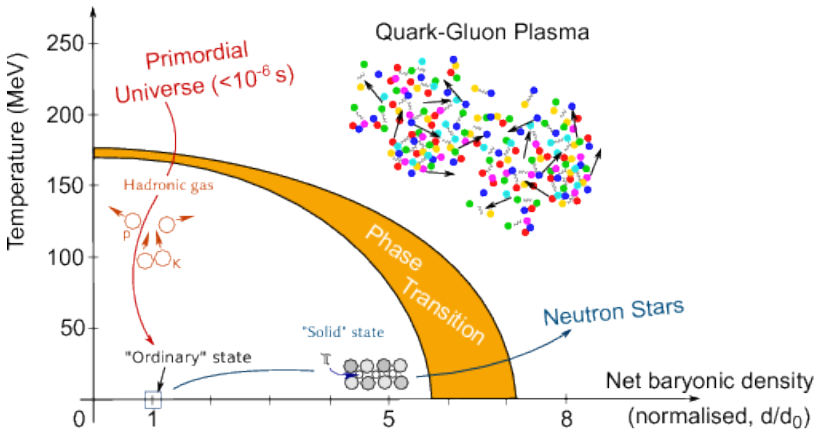

Figure 1: Phase diagram of QCD matter, showing the transition at $T_c = 150 - 190$ MeV from ordinary confined matter to a deconfined QGP state. The trajectory of the early universe (in red) shows the decrease in temperature that took matter from a hadronic gas to its "ordinary" state. This plot, created by the ALICE Collaboration, also includes the temperatures and baryon densities of other forms of matter, like solids and neutron stars, in comparison with the very high-temperature and density QGP.

1.2.1 Experimental evidence of QGP

There are three pillars of evidence for QGP formation in experimental settings: heavy quarkonium suppression, jet production and quenching, and elliptic flow, with this last one being most relevant to this project.

Quarkonium suppression: Extreme color fields created inside the plasma can screen heavy quarkonia, which are mesons formed from heavy quark-antiquark pairs. Screening causes the valence quarks to dissociate and form open heavy flavor mesons before they can escape the QGP and undergo standard decay in the surrounding vacuum (which would produce detectable signatures in the form of lepton pairs) [2]. As the QGP gets hotter, the free partons can screen at smaller and smaller distances, though at any temperature, the weakly-bound quarkonia will be more suppressed than the tightly-bound quarkonia. Thus, measuring suppression of different quarkonia points to the length scale at which the QGP starts to screen, which in turn informs about the temperature of the system [5].

Jet quenching: The production of jets involves the high-momentum scattering of quarks and gluons that produces narrow, back-to-back sprays of hadrons. Head-on collisions between partons generate bursts of energy that quickly condense into "jets" of pions, kaons, and other particles. These jets are formed in pairs, one of which gets weakened or even extinguished if it has to traverse the dense fireball produced in a heavy ion collision; the "quenched" jet experiences significant energy loss due to interactions with the quark- and gluon-rich medium. The jets are considered hard probes in that they are strongly interacting but moving fast enough not to be completely absorbed by the medium. The amount of quenching, the orientation and composition of the jets, and the manner in which the jets transfer energy and momentum all reveal information about the contents of the fireball and therefore the properties of the QGP [6].

Elliptic flow: An important feature of a hot, dense, strongly-coupled QGP is the azimuthal anisotropy of charged particles produced in an inelastic collision between two nuclei. Non-central nuclear collisions produce an almond-shaped overlap region, as shown in the top of Fig. 2. Note that the spherical approximations for the colliding nuclei in this part of the figure are not entirely accurate; these shapes do not account for the highly relativistic speeds at which the collisions are occurring and hence in reality, the incident nuclei should have more flattened pancake-shaped cross sections. The strong rescattering of partons in the initial state of the collision leads to the formation of local thermal equilibria, which in turn causes the buildup of non-uniform pressure

gradients in the almond. This drives anisotropic expansion of the plasma such that outgoing particles are emitted preferentially along the direction of the impact parameter vector between the two nuclei (the horizontal offset between the spheres) as shown in the lower half of Fig. 2.

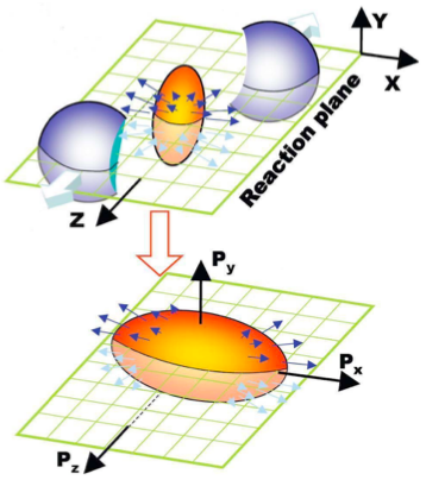

Figure 2: Geometry of a non-central heavy ion collision. The initial spatial anisotropy (exemplified by the almond-shaped overlap in the top half) results in a final momentum anisotropy for the outgoing particles (conveyed in the bottom half).

Flow has final state observables (e.g. pions formed late in the evolution), but the final momentum distribution preserves information from early in the collision because of its intrinsic connection with the initial spatial anisotropy. The medium's high opacity and the elliptical distribution of emitted hadrons are both more characteristic of a fluid; if the QGP behaved like a gas, the hadrons would emerge uniformly in all directions from a less opaque plasma. Continuing to study flow in this system, especially elliptic flow, will provide more insight into the QGP's bulk properties (e.g. viscosity, equation of state, etc.) [2].

1.3 Experimental facilities

The aforementioned signatures of QGP formation are studied at the Large Hadron Collider and at Brookhaven National Lab's Relativistic Heavy Ion Collider, in the Compact Muon Solenoid (CMS) and the Solenoidal Tracker at RHIC (STAR) experiments shown in Fig. 3, respectively; other experiments at these colliders focus on a wide variety of other pressing questions in physics. In both general purpose detectors, violent collisions between highly relativistic heavy nuclei generate femtoscopic fireballs of melted nucleons that can send hundreds of particles flying out into the surrounding trackers and calorimeters. In particular, the heavy ion collisions of interest in these experiments rely on lead and gold nuclei, which are capable of reaching the extreme pressure and temperature conditions needed to create a QGP thanks to their relatively high densities. In any given heavy ion collision, the two nuclei (either lead or gold in the case of my research) collide with each other, forming a hot, dense phase that is thought to be a QGP. Approximately 10^{-23} seconds after the initial collision, the initial QGP phase cools and condenses into a hadronic gas. These hadrons continue to cool and spread out until they cease interacting with each other, eventually reaching the detectors roughly 10^{-9} seconds after the collision took place[7].

1.3.1 Compact Muon Solenoid

One of two general purpose detectors at the LHC, the CMS experiment is pursuing a broad range of physics questions, from the Standard Model and the Higgs boson to searches for extra dimensions and dark matter candidates. Following a high energy collision of two heavy nuclei in the heart of the detector, the innermost

silicon trackers first reconstruct the paths of the charged particles coming out of the collision. Next, the two calorimeters measure the energy of the outgoing particles; the electromagnetic calorimeter does so for electrons and photons using $PbWO_4$ crystals, while the hadron calorimeter detects any particle made of quarks or gluons. The previous parts are all enclosed in a superconducting solenoid that generates a 3.8 T magnetic field. Lastly, the iron magnet return yoke stops all remaining particles from reaching the expansive muon chambers dedicated to stopping the very weakly interacting muons.

1.3.2 Solenoidal Tracker At RHIC

While CMS investigates a variety of scientific inquiries, STAR is designed to focus on the formation and behavior of high-density, strongly-interacting matter. STAR is schematically similar to CMS in its concentric arrangement of trackers (both silicon and gaseous), an electromagnetic calorimeter, and a solenoidal magnet around the beam interaction region. The core of the STAR detector is the Time Projection Chamber (TPC), which serves as the primary tracking device, measuring particles' tracks, momenta, and ionization energy loss [8]. The TPC is in turn surrounded by the Time Of Flight detector, which measures the time of flight (no surprise there) that can then be used with the corresponding transverse momentum to identify particles. These are all contained within a solenoidal magnet operating at 0.5 T.

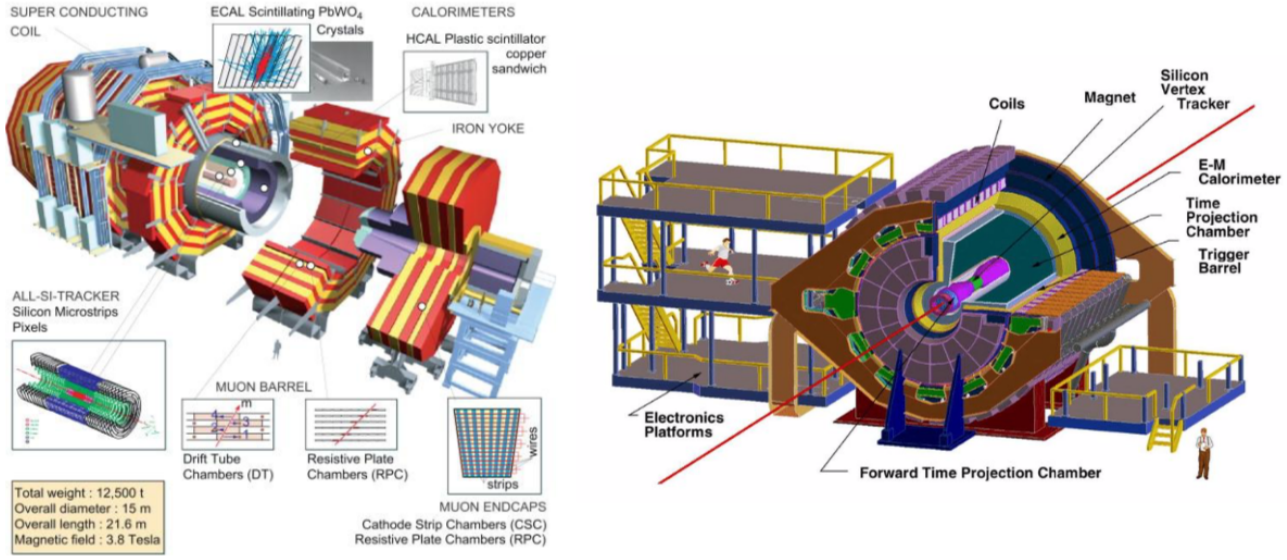

Figure 3: Schematic of the Compact Muon Solenoid (left, source: CMS Collaboration) and the Solenoidal Tracker at RHIC detectors (right, source: STAR Collaboration).

2 The Glauber Model

Given the complexity of heavy ion collisions, it is natural to wonder about the number of incident nucleons that actually participate in a particular interaction and the shape of the overlap between the nuclei. The phenomenological techniques that have been developed to figure out these quantities for such femtoscopic many-body systems are known as Glauber models, named after the pioneering and Nobel Prize-winning theoretical physicist Roy Glauber (1925-2018). The heavy ion physics community does use a variety of other models to visualize and analyze these high energy events, including hydrodynamics, Ultra-relativistic Quantum-Molecular-Dynamics (UrQMD), parton cascade models (which more prominently feature perturbative QCD), and multi-phase transport models. All of those are notably more complicated to formulate and readily comprehend, which is why I chose to implement a Glauber model approach to my ROOT simulations of ultra-relativistic Pb+Pb and Au+Au collisions for this project.

The Glauber model treats collisions between nuclei as independent sequences of individual nucleon-nucleon interactions, getting its theoretical basis from quantum theories about the scattering of composite particles [9]. Since the femtometer scales on which these collisions occur preclude direct observation, the impact parameter (a vector $\vec{b}$ representing the offset between the centers of the two nuclei, see Fig. 4), the number of nucleons that experience at least one nucleon-nucleon collision (number of "participants", N_{part}), and the number of binary nucleon-nucleon collisions (N_{coll}) all must be estimated from experimental data using these theoretical methods. Together with the impact parameter b, the quantities N_{part} and N_{coll} characterize the centrality of the collision—i.e. its size, shape, and the degree of overlap between the incident nuclei at the interaction point.

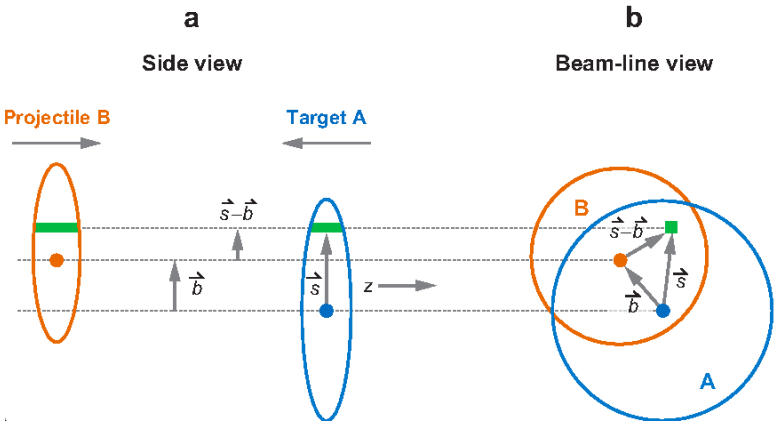

Figure 4: Schematic of a collision between two nuclei (Projectile B and Target A) which in this case are of different sizes and therefore different species. The offset between their two centers is represented by the impact parameter vector $\vec{b}$. The interaction is illustrated in both side view and beam-line view to show how the overlap forms. The green rectangles represent flux tubes that overlap during the collision, being located at a displacement $\vec{s}$ from the center of Target A [9].

For a Monte Carlo Glauber (MCG) model, the only required inputs are a randomly generated impact parameter (hence the Monte Carlo part), a measured nuclear density function $\rho(r)$, and a measured inelastic nucleon-nucleon cross-section $\sigma_{\text{inel}}^{\text{NN}}$ [10]. This last parameter is calculated as the total nucleon-nucleon cross-section minus the elastic nucleon-nucleon cross-section, both of which are experimentally measurable quantities. The focus is on inelastic collisions because those actually produce new particles, as opposed to elastic collisions in which the nucleons simply scatter off each other without fragmenting. The specific value of $\sigma_{\text{inel}}^{\text{NN}}$ essentially relates to how big a nucleon is, which in turn depends on its energy in that higher center-of-mass energies are associated with larger cross-sections; this could be due to the stronger interactions that occur as the mass and charge of the nucleus is increasingly concentrated/condensed at higher energies. It is used to determine how close the nucleon trajectories need to be in order for a collision to occur, a condition discussed in a later section. Since it is based purely on nuclear geometry, this type of modelling is fairly simplistic and does make some fundamental assumptions that may or may not accurately reflect reality. Here, the nucleons are assumed to follow straight line trajectories and $\sigma_{\text{NN}}^{\text{inel}}$ is taken to be independent of any previous collisions, and therefore the nuclei are modelled as just passing through each other.

2.1 Woods-Saxon nuclear density function

The only input values that must be known prior to constructing and utilizing an MCG model are $\sigma_{\text{NN}}^{\text{inel}}$ and the parameters for the nuclear density function, in this case the Woods-Saxon function shown in Fig. 5 and

represented by the equation below:

$$\rho(r) = \rho_0 \left[1 + \exp\left[\frac{r - r_0}{a}\right]\right]^{-1}$$

This distribution governs the density of nucleons as a function of distance from the center of the nucleus, where ρ_0 is the nuclear density at the center, r_0 is the nuclear radius, and a is the skin depth (which characterizes how sharp the edge of the nucleus is). The Woods-Saxon distribution becomes a step function in the hard sphere limit (as a goes to zero) since the nucleus is now being treated as a sphere-shaped object with well-defined boundaries instead of diffuse ones.

The radial probability function is calculated by multiplying the Woods-Saxon function by the distance from the center of the nucleus squared (r^2). This equation is then used to randomly distribute the nucleons that will be accelerated towards each other in any given run of the model. The x, y, and z coordinates for each of the 416 nucleons in Pb+Pb, or 394 nucleons in Au+Au, are randomly determined according to $\rho(r) \cdot r^2$, which is shown in Fig. 5 for a lead nucleus.

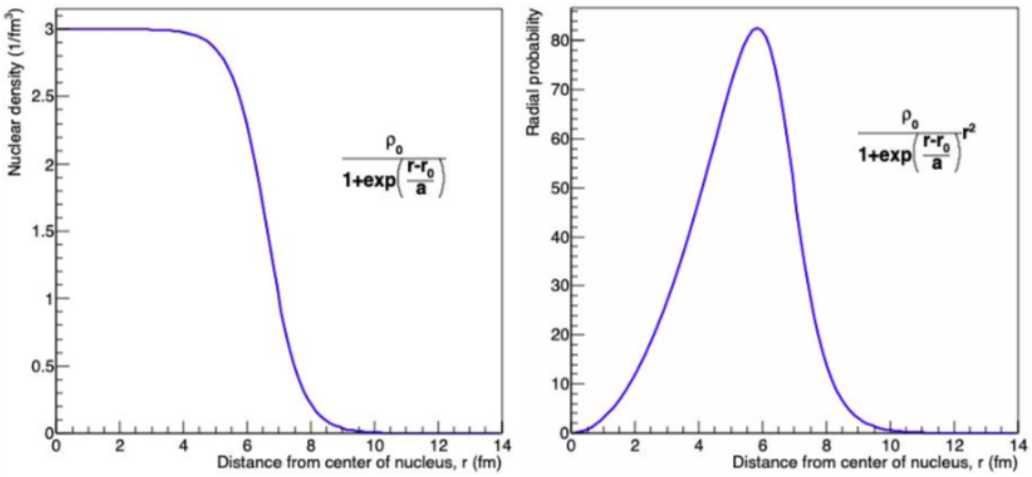

Figure 5: Radial density function for a Pb nucleus ($r_0 = 6.62$ fm, $a = 0.542$ fm) assuming a Woods-Saxon distribution (left), and the corresponding radial probability function (right).

2.2 Impact parameter generation

After the nucleons in the simulation have been randomly distributed in accordance with the Woods-Saxon function, all of the constituents of one nucleus are shifted laterally by the impact parameter. A specific value of b is drawn from the distribution (shown in Fig. 6)

$$\frac{d\sigma}{db} = 2\pi b\,,$$

indicating that the probability of a given impact parameter follows a linear trend. Selecting an impact parameter for a hypothetical heavy ion collision is analogous to trying to hit a bullseye, in that the target area is proportional to the probability. Thus, the probability of a head-on, central collision (approaching $b = 0$) is much lower than probability of a more peripheral collision (large b). In reality, the impact parameter vector can point in any direction because of the assumed spherical symmetry of the system, but for convenience the offset is taken to be in the positive $\hat{x}$ direction in this model.

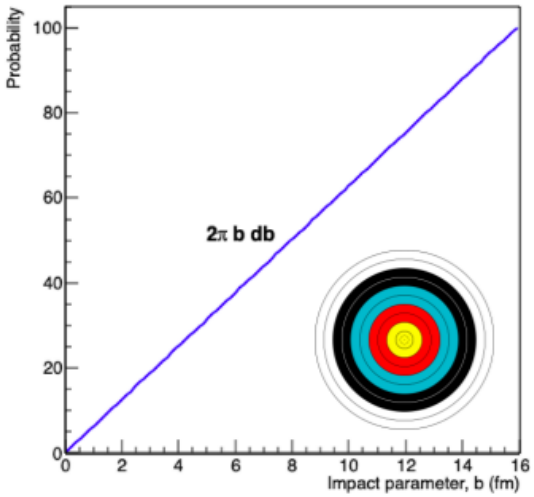

Figure 6: Distribution of impact parameter values for heavy ion collisions. For any given nucleus-nucleus collision, a value is drawn from this distribution to determine how close the trajectories of the incoming nuclei in this simulated event will be.

In order for any two nucleons to experience a binary collision, the following condition for the distance d between them must be satisfied:

$$d \leq \sqrt{\sigma_{\text{inel}}^{\text{NN}}/\pi}$$

For a collision between Nucleus A and Nucleus B, every nucleon in A is checked against every nucleon in B to determine if their randomly generated coordinates will lead to a nucleon-nucleon collision; that is, if the distance between their respective randomly generated coordinates is less than the square root of the inelastic nucleon-nucleon cross-section over pi, they will interact and are subsequently labeled "participants". Every nucleon that experiences at least one binary collision is marked by a darker color in Fig. 7 to distinguish it from the spectator nucleons (i.e. those that pass through the interaction region without colliding or interacting at all). Note the almond-shaped overlap region visible from this $\hat{z}$-direction (beam-line) view; as mentioned in the preceding discussion of elliptic flow as evidence of QGP formation, the particles emitted along the short axis of the almond will experience the greatest momentum boost.

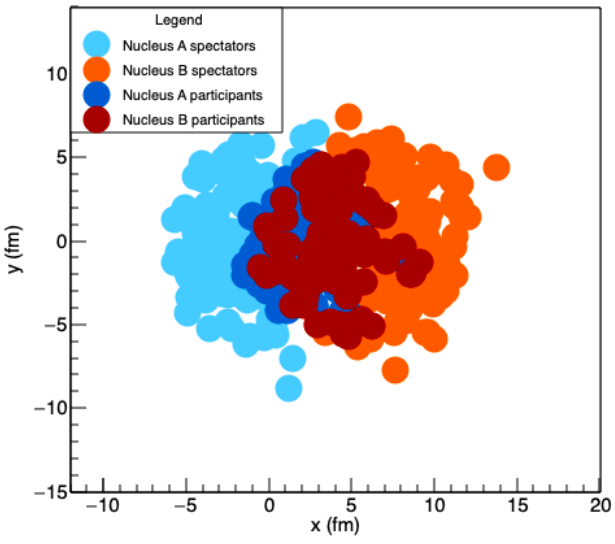

Figure 7: Distribution of all 416 nucleons in a sample Pb+Pb collision at $\sqrt{s_{\text{NN}}} = 2.76$ TeV with $\sigma_{\text{inel}}^{\text{NN}} = 65$ mb and $b = 6$ fm, with the participating nucleons from each nucleus being shown in darker colors.

2.3 Resulting histograms and correlations

After running 10^6 pseudo-experiments of the model, about 75% of which resulted in at least one binary nucleon-nucleon collision, the following distributions of b, N_{part}, and N_{coll} were generated. The impact parameter histogram shows how the number of counts of b increases linearly with the value of b itself (as expected given the manner in which b was generated) up until about twice the nuclear radius, at which point the probability of any nucleon-nucleon collisions starts to drop off. However, it is not a sharp drop off because the nuclei are not hard spheres, but instead are a bit more diffuse, as alluded to in the nucleon distribution plot in Fig. 7. The N_{part} histogram does have a sharp drop off since there is a well-defined maximum number of participants: 416 for Pb+Pb; and 394 for Au+Au. These distributions of resulting b and N_{part} values for the roughly 750,000 trials that had at least one binary nucleon-nucleon collision are shown in Fig. 8 below.

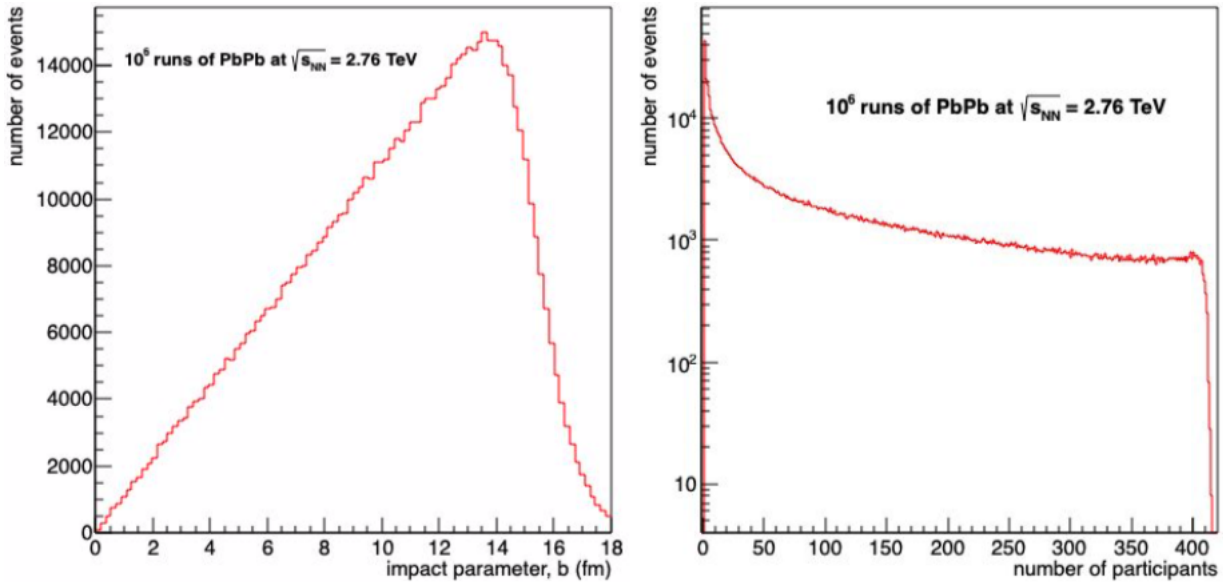

Figure 8: Histograms of resulting impact parameter values (left) and numbers of participants (right) for trials of Pb+Pb at $\sqrt{s_{\text{NN}}} = 2.76$ TeV that resulted in at least one nucleon-nucleon collision.

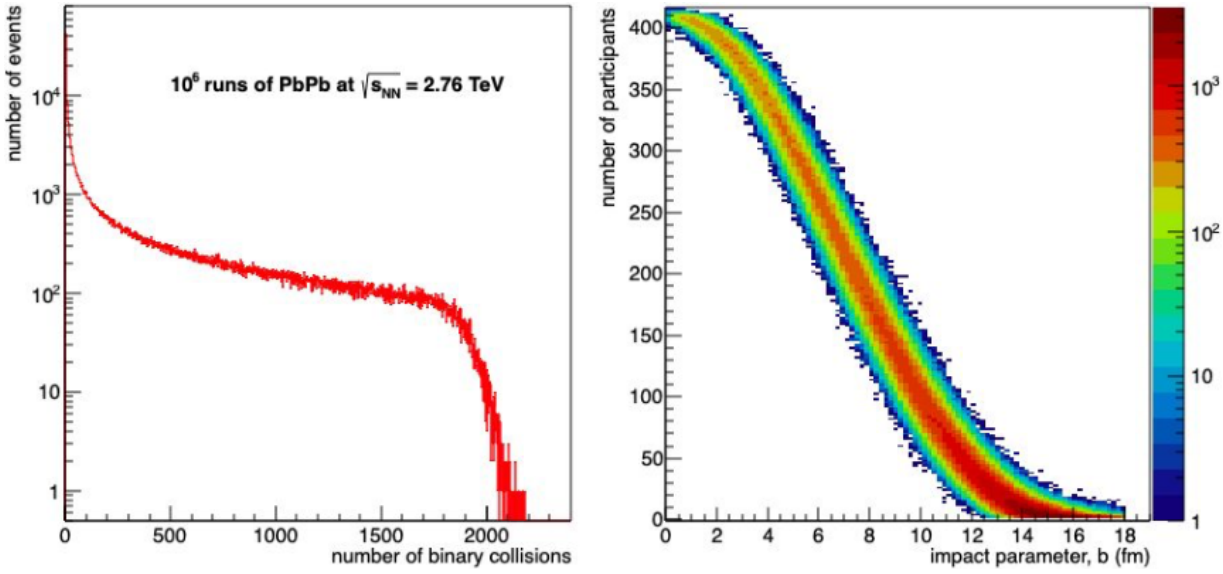

Figure 9: Histogram of resulting N_{coll} for Pb+Pb events that had $N_{\text{coll}} \geq 1$ (left), and the correlation between impact parameter and number of participants (right), in which the color scale on the far right represents the number of events/counts.

The N_{coll} histogram shown on the left in Fig. 9 exhibits a characteristic "horseback" shape. As expected, there is a positive relationship between N_{part} and N_{coll}, since a greater number of interacting nucleons would logically be associated with a greater number of nucleon-nucleon collisions occurring. There is a clear negative correlation between the impact parameter and both N_{part} (shown on the right in Fig. 9) and N_{coll}; that is, a smaller impact parameter corresponds to a more central collision that sees higher numbers of participants and binary collisions due to the increased overlap between the nuclei. In the correlation plot, one can clearly see a hot spot (i.e. the most probable outcome of a run, the dark red portion) at high b, low N_{part}, and low N_{coll}. None of the variables noted previously—b, N_{part}, or N_{coll}—can be measured experimentally, so in order to more directly compare this model against real experimental data, a particle production model must be incorporated into the existing MCG simulation. This involves the calculation of a centrality variable via a negative binomial distribution (NBD).

2.4 Particle production model and the negative binomial distribution

Centrality variables are measurable quantities that relate to how head-on a given nucleus-nucleus collision is. CMS uses the total transverse energy ΣE_{T} (perpendicular to the beam direction), while STAR uses the particle multiplicity $dN_{ch}/d\eta$ at mid-rapidity (number of particles produced around $\eta = 0$, which corresponds to about $\pm 30^{\circ}$ from perpendicular to the beam line). In a detector, these are measured as tracks in the trackers (for the multiplicity) or as energy deposited in the calorimeters (for ΣE_{T}). Both are calculated using an NBD, expressed in terms of parameters μ and k using gamma functions as:

$$\frac{\Gamma(k+n)}{k!\Gamma(n)} \cdot \frac{(\mu/k)^n}{(1+\mu/k)^{n+k}}$$

In this expression, n represents the amount of transverse energy (the energy of particles with high p_{T}) or the number of particles produced in a particular nucleon-nucleon collision, μ is the mean E_{T} or multiplicity, and k is a parameter relating to the width of the distribution [10]. The total transverse energy or multiplicity distribution is obtained by convolving the NBD with the N_{coll} histogram. For both CMS and STAR analyses, a value is randomly drawn from the NBD to determine the amount of transverse energy or the number of particles produced in a single nucleon-nucleon collision. This random drawing is repeated N_{coll} times and summed up to calculate the ΣE_{T} or the total $dN_{ch}/d\eta$ for a particular nucleus-nucleus collision that had exactly N_{coll} nucleon-nucleon collisions. That entire process is then repeated for however many events out of the 10^6 pseudo-experiments had that specific value of N_{coll}. Once those calculations have been completed, the generated ΣE_{T} or $[dN_{ch}/d\eta]_{\eta=0}$ distribution can be compared with and fit to experimental data by optimizing the NBD parameters: μ, k, and the normalization/scaling factor.

2.4.1 Parameter fitting for the NBD

Starting with Pb+Pb at $\sqrt{s_{\text{NN}}} = 2.76$ TeV, the best values of μ, k, and the normalization factor were determined by minimizing χ^2 between the generated and experimental ΣE_{T} distributions. The χ^2 value is a measure of how good a fit is and is calculated as follows:

$$\chi^2 = \sum_{\text{all } i} \frac{(O_i - E_i)^2}{E_i}$$

where O_i is the observed (generated) value and E_i is the expected (experimental) value of ΣE_{T}. The data were only fit for 0.5-5 TeV instead of the full 0-5 TeV range, in order to avoid the inefficiencies associated with the most peripheral collisions (at total transverse energies of less than 0.5 TeV). First, the χ^2 values were calculated in a few coarse passes over a broad range of μ and k (shown on the left in Fig. 10). These scans of the parameter space involved choosing particular values for μ and k (assuming a constant normalization in this stage of the fitting) and creating a ΣE_{T} distribution with those values. This generated distribution was then compared with

the experimental ΣE_{T} data from CMS by determining the total χ^2. Each colored square in the plots in Fig. 10 represents the resulting χ^2 (shown by the numbers in the center of each square) for one pair of μ and k (listed on the axes). As previously mentioned, each pass does this for a range of parameter values, looping through nine pairs of μ and k for the initial rounds of fitting. Next, the scaling of the generated ΣE_{T} histogram was varied to find the best value of the normalization factor, since the number of events in the real dataset was not necessarily equal to the number of pseudo-experiments in the model. This was followed by finer scans of the μ and k parameter space to find a local minimum in χ^2, i.e. over smaller ranges in μ and k with more pairs of values being tested (36 compared to 9 in the first few passes). The goal of the parameter fitting was to reach a χ^2 around 100, since the system has 98 degrees of freedom from 100 bins in the histogram of the centrality variable minus two parameters. This was achieved in the final scan with a χ^2 of approximately 105, shown on the right in Fig. 10, pointing to $\mu = 1.39$, $k = 0.45$, and a scaling factor of 0.041 as the values that best match the generated distribution to the CMS data. These values were then put into the negative binomial distribution that is included in the particle production piece of the model. The plot showing the updated fit between the experimental data and my MCG model for Pb+Pb at $\sqrt{s_{\mathrm{NN}}} = 2.76$ TeV, with centrality classes shown, is given in Fig. 11 and discussed in the following section.

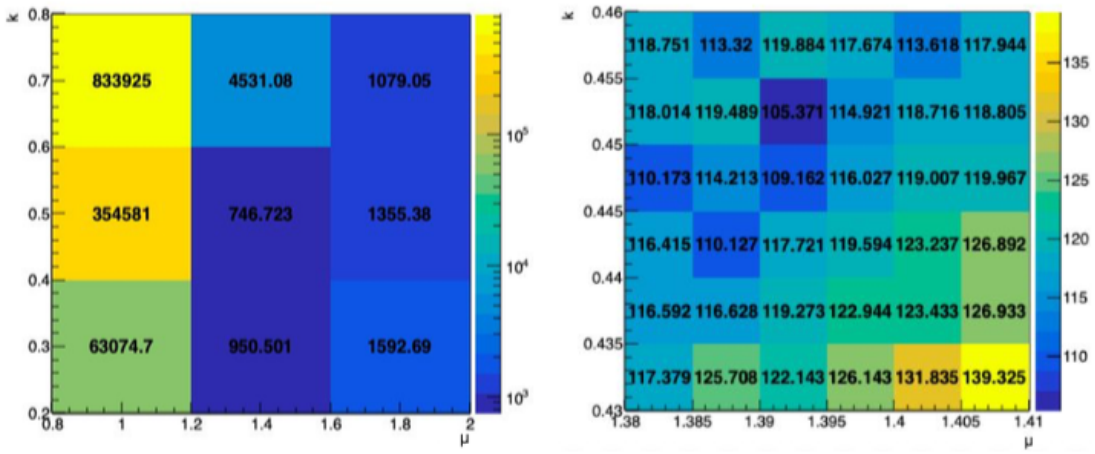

Figure 10: An initial coarse scan of the parameter space (left), and the final scan of the space (after determining the best scaling factor) that produced the values of μ, k, and normalization that were ultimately used (right).

2.5 Determining centrality classes

Calculations of centrality variables are used to create centrality classes, which divide up the results of a particular collision type into fractions of the total integral of the centrality variable distribution. The convention is that 0% represents the most central collision and 100% corresponds to the most peripheral. Cuts are made in total transverse energy (for Pb+Pb data from CMS) or in particle multiplicity (for Au+Au data from STAR, referred to as refMult in subsequent tables) to divide the integral in 5% increments, and the ranges corresponding to each percentile are noted so average values of other variables (like N_{part}) can be determined as functions of centrality. Fig. 11 shows the generated ΣE_{T} histogram using the final NBD parameters (listed in the previous section) in comparison with provided CMS data for Pb+Pb at $\sqrt{s_{\mathrm{NN}}} = 2.76$ TeV. The centrality classes from 0% to 70% based on cuts in ΣE_{T} are marked by the green dashed lines, shown for the 0% to 50% classes in 5% increments, then in 10% increments for the remainder as the spacing between classes decreases.

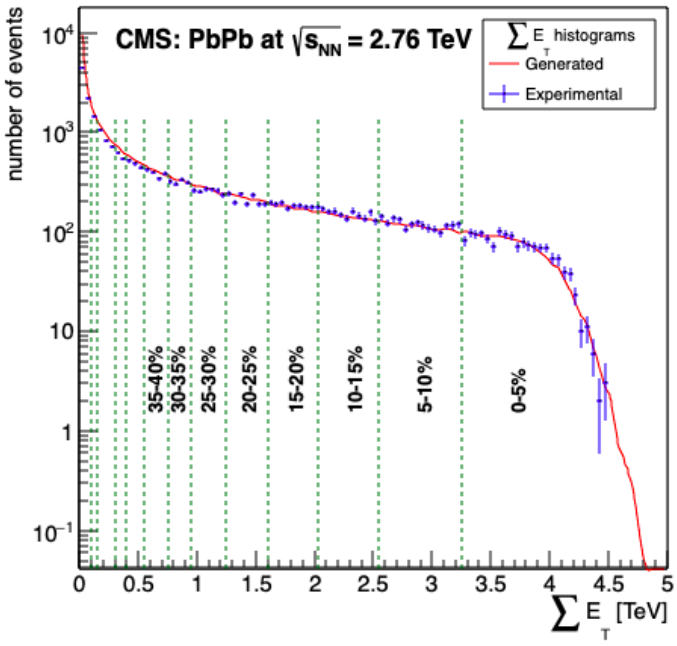

Figure 11: Final ΣE_{T} histogram for Pb+Pb at 2.76 TeV (red line) with centrality classes (green dashed lines) and CMS data for comparison (blue points with error bars) [11].

3 Eccentricity and overlap area calculations

Both the eccentricity ϵ and overlap area S characterize the almond-shaped overlap region in the initial state of the collision and are therefore geometric quantities of interest to . The specific shape of the overlap area can be irregular, while its orientation is determined by the impact parameter vector and fluctuates from event to event. The eccentricity quantifies the initial spatial anisotropy (i.e. the shape and orientation) that ultimately results in the anisotropic final momentum distribution for emitted particles that is observed in elliptic flow.

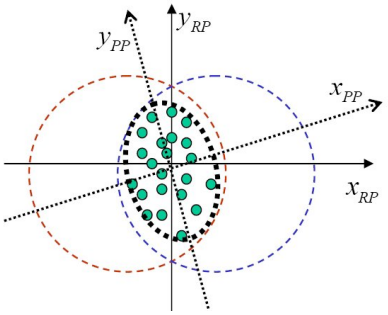

Figure 12: Coordinate axes for the reaction plane (RP) and the participant plane (PP) shown with respect to the overlap between two nuclei, with participating nucleons being shown in green.

Both geometric quantities, ϵ and S, are defined in two coordinate systems, shown in Fig. 12: the reaction plane and the participant plane. The reaction plane is determined by the beam direction and the impact parameter vector, shown above as the x_{RP} and y_{RP} axes. Conversely, the participant plane is determined by the beam direction and a rotated $x'y'$ frame that aligns itself with the participants—note how the x_{PP} and y_{PP} axes line up better with the green participating nucleons in Fig. 12. The planes are different because the spatial distribution of participating nucleons is not necessarily symmetric with respect to the reaction plane and the direct overlap between the two nuclei. Furthermore, the true reaction plane cannot be known experimentally, which is why the participant versions are more commonly used. This difference translates into the following

equations, where the participant definitions have an extra covariance term that rotates the coordinate system depending on the locations of the participants:

$$\epsilon_{\mathrm{RP}} = \frac{\sigma_y^2 - \sigma_x^2}{\sigma_y^2 + \sigma_x^2}\,, \quad \epsilon_{\mathrm{part}} = \frac{\sqrt{(\sigma_y^2 - \sigma_x^2)^2 + 4\sigma_{xy}^2}}{\sigma_y^2 + \sigma_x^2}$$

$$S_{\mathrm{RP}} = \pi\sqrt{\sigma_x^2\sigma_y^2}\,, \quad S_{\mathrm{part}} = \pi\sqrt{\sigma_x^2\sigma_y^2 - \sigma_{xy}^2}$$

in which the variances and the covariance are calculated as $\sigma_x^2 = \langle x^2\rangle - \langle x\rangle^2$, $\sigma_y^2 = \langle y^2\rangle - \langle y\rangle^2$, and $\sigma_{xy} = \langle xy\rangle - \langle x\rangle\langle y\rangle$ [12]. By definition, ϵ_{part} can only have positive values (while ϵ_{RP} can be negative) and represents the maximum calculated eccentricity for a given collision regardless of the direction of the initial b vector.

3.1 Relevance to elliptic flow analysis

These calculations can be added to the existing Glauber model, which in its current state provides the most basic information about the heavy ion collision and its aftermath, in order to learn more about the initial state geometry of each nuclear collision. Given the eccentricity and overlap area's relevance to the spatial anisotropy of the initial nuclear overlap (by quantifying its sharp, elliptical shape and size), both quantities can be used in elliptic flow analysis; this is because a characteristic feature of a strongly-coupled QGP is the azimuthal anisotropy of emitted charged particles. The eccentricity in particular, which can be calculated event-by-event using this MCG approach, is helpful in analyses that determine the strength of the elliptic flow, known as v_2. Elliptic flow is quantified using the correlations in azimuthal angle between detected particles [13], while v_2 specifically is given by the second term in a Fourier expansion of the particles' invariant yield; this invariant yield refers to the integrated flow of observed particles over a broad range of rapidity (i.e. angular separation of the outgoing particles related to their relativistic motion) and transverse momentum [14]. Calculations of ϵ and S would be useful for characterizing various collision shapes across different event classes and for measurements of elliptic flow of heavy mesons. Knowing the eccentricity would also be useful for analysis of eccentricity-scaled elliptic flow, $v_2/\epsilon_{\mathrm{part}}$; dividing v_2 by the eccentricity can potentially remove the dependence of the collective flow and anisotropy parameter on the initial nucleus-nucleus collision area, thereby enabling better comparison of results across numerous centralities, colliding species, and center-of-mass energies. Additionally, strongly anisotropic collective quark flow has been observed for light quarks, but current experimentation is looking into whether heavy quarks undergo hydrodynamic flow as well since elliptic flow reveals key information about the initial conditions of the collision.

4 Results

4.1 Au+Au at $\sqrt{s_{\mathrm{NN}}} = 200$ GeV

For the initial calculations of ϵ and S, the collision type was switched from Pb+Pb at $\sqrt{s_{\mathrm{NN}}} = 2.76$ TeV to Au+Au at $\sqrt{s_{\mathrm{NN}}} = 200$ GeV since the paper in which the relevant equations had been found focused on that type of heavy ion collision [12]. The behavior of the average reaction-plane and participant eccentricities as functions of the average number of participants was found to be consistent with expectations from published plots, with Fig. 13 showing this expected behavior. The monotonic trend observed for the average ϵ_{part} is not seen with ϵ_{RP}; the drop-off occurs because for very peripheral collisions (low $\langle N_{\mathrm{part}}\rangle$, high b) there are larger fluctuations in the shape and orientation of the already small nuclear overlap and rotating the coordinate system to better line up with the participants (as done for ϵ_{part}) counteracts that. Additionally, note that at high numbers of participants (high $\langle N_{\mathrm{part}}\rangle$, low b) the two coordinate systems and calculation methods for ϵ are more consistent with each other than in the low N_{part} case; this is fairly unsurprising since for those types of collisions the high degree of overlap between the nuclei means there is not a lot of variation in shape

and orientation of the participants from event to event. Additionally, this constitutes another example of the generally higher discrepancy and uncertainty associated with peripheral collisions.

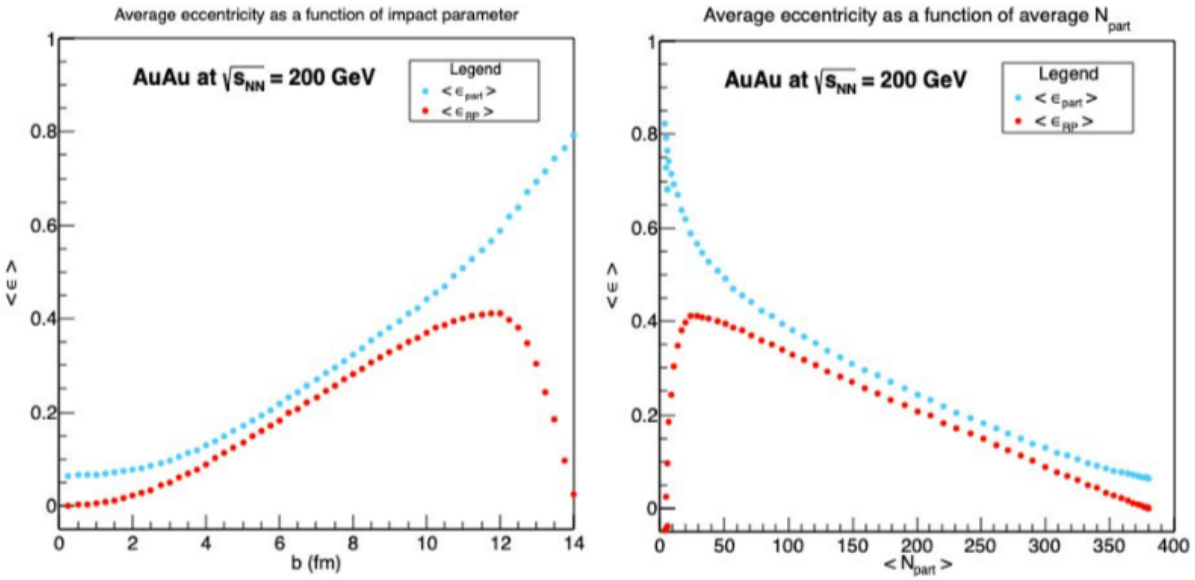

Figure 13: Average ϵ_{RP} and ϵ_{part} as a function of b (left) and average N_{part} (right) for 200 GeV Au+Au.

Centrality	**0-5%**	**5-10%**	**10-15%**	**15-20%**	**20-30%**	**30-40%**	**40-50%**	**50-60%**	**60-70%**
refMult	≥566	447-566	353-447	278-353	168-278	97-168	52-97	26-52	13-26
b_{avg} (fm)	2.26	4.02	5.21	6.22	7.38	8.72	9.87	10.89	11.79
N_{part}	351.3	299.9	253.8	213.8	165.9	114.6	76.34	48.22	29.02
ϵ_{RP}	0.0318	0.0912	0.145	0.192	0.247	0.309	0.356	0.382	0.389
ϵ_{part}	0.0854	0.131	0.180	0.227	0.286	0.360	0.425	0.487	0.557
S_{RP} (fm^2)	26.0	23.4	20.9	18.6	15.9	12.8	10.3	8.22	6.43
S_{part} (fm^2)	25.9	23.3	20.8	18.5	15.7	12.6	10.0	7.84	5.92

Table 1: Calculated eccentricities and overlap areas for a range of centrality classes (based on cuts in multiplicity) for Au+Au at $\sqrt{s_{\mathrm{NN}}}$ = 200 GeV. Except for the refMult (i.e. number of particles produced) ranges used to determine the centrality classes, all other reported values (b_{avg} through S_{part}) in the table are averages.

Centrality	**0-5%**	**5-10%**	**10-15%**	**15-20%**	**20-30%**	**30-40%**	**40-50%**	**50-60%**	**60-70%**
b_{min} (fm)	0.0	3.3	4.7	5.8	6.7	8.2	9.4	10.6	11.6
b_{max} (fm)	3.3	4.7	5.8	6.7	8.2	9.4	10.6	11.6	12.5
N_{part}	352	295	245	204	154	104	65.1	36.8	18.8
ϵ_{RP}	0.0446	0.120	0.183	0.233	0.292	0.348	0.389	0.405	0.398
ϵ_{part}	0.0818	0.145	0.204	0.254	0.318	0.380	0.433	0.473	0.497
S_{RP} (fm^2)	23.4	20.5	18.0	16.0	13.5	10.9	8.69	6.78	5.07
S_{part} (fm^2)	23.4	20.5	18.0	16.0	13.5	10.9	8.65	6.73	5.05

Table 2: Average eccentricities, overlap areas, and number of participants for various centrality classes for Au+Au at $\sqrt{s_{\mathrm{NN}}}$ = 200 GeV, from T. Hirano and Y. Nara [12].

Table 1 shows the calculated eccentricities and overlap areas, in addition to the average impact parameter and average number of participants, for a variety of centrality classes. This table was meant to reproduce the values shown in a similar table from Hirano and Nara's paper (Table 2 above). The average impact parameter in Table

1 falls within the range of b listed in Table 2 for all centrality classes, while the two key variables of $\langle N_{\text{part}} \rangle$ and $\langle \epsilon_{\text{part}} \rangle$ are consistent with each other between the two tables for more central collisions. The agreement between the results of my calculations and those provided by Hirano and Nara becomes weaker for more peripheral collisions, which is perhaps to be expected since less central collisions are generally associated with higher degrees of uncertainty and fluctuation. Despite any differences in exact values, the appropriate trends in the data are preserved; collisions at small impact parameter are associated with high N_{part}, large overlap areas, and small eccentricities, while less central collisions at large impact parameter have comparatively lower N_{part}, smaller overlap areas, and large eccentricities.

While the values do not perfectly agree, any appreciable discrepancies can be attributed to two main differences in methodology and construction of the MCG models. First, Hirano and Nara assume a finite size profile for the nucleons, whereas the modelling done in this project uses a delta function for the nucleon profile. Hirano and Nara express a nuclear density function that assumes a Woods-Saxon distribution (ρ_{WS}) with a delta function profile as

$$\rho(\vec{x}) = \int \delta^{(3)}(\vec{x} - \vec{x}_0)\rho_{WS}(\vec{x}_0)d^3\vec{x}_0 \,,$$

while their finite size profile version is expressed as

$$\rho(\vec{x}) = \int \Delta(\vec{x} - \vec{x}_0)\rho_{WS}(\vec{x}_0)d^3\vec{x}_0 \quad \text{where} \quad \Delta(\vec{x} - \vec{x}_0) = \frac{\theta(r_N - |\vec{x} - \vec{x}_0|)}{V_N}$$

with $V_N = \frac{4\pi r_N^3}{3}$ and $r_N = \sqrt{\sigma_{\text{inel}}^{\text{NN}}/\pi}$ [12]. Since their nuclear density function is no longer the same as a Woods-Saxon distribution, they also use different input parameter values; for Au+Au, they use $\rho_0 = 0.1695$ fm^{-3}, $r_0 = 6.42$ fm and $a = 0.44$ fm, while my table was filled using $r_0 = 6.38$ fm and $a = 0.535$ fm (same ρ_0) [12]. This apparent discrepancy in the two methods of distributing the nucleons ultimately had little effect on the resulting calculations; the more consequential methodology difference came from a perceived inconsistency between the theoretical and the experimental approach to the nuclear collision modelling. As theorists, Hirano and Nara determined their centrality classes based on cuts in impact parameter and not in terms of particle multiplicity. This is not experimentally feasible because the offset between the nuclei in any collision is not controllable, nor is the impact parameter a quantity that can actually be measured. For the sake of being thorough, I did redo the calculations of the average values based on cuts in b instead of refMult, and the values were much closer—for example, it brought the average N_{part} for the 60-70% centrality class down from 29 to 23 (compared to Hirano and Nara's value of 19)—so it is clear that the choice of centrality variable matters. The overestimation of the number of participants likely also relates to the lack of exclusion in my model; that is, when randomly distributing the nucleons, my simulation does not check that each nucleon is initially at least 1 fm from the other constituents of the nucleus it belongs to, thereby allowing the nucleons to be closer together and therefore more likely to interact.

4.2 Pb+Pb at $\sqrt{s_{\text{NN}}} = 2.76$ TeV

As with the Au+Au collisions, the behavior of the average reaction-plane and participant eccentricities as functions of N_{part} are consistent with expectations, in this case from direct experimental datasets. The ϵ vs b plot for Pb+Pb shown on the left in Fig. 14 shows the same behavior as for Au+Au in that both definitions of ϵ agree reasonably well at lower b but diverge for higher impact parameters, and that $\langle \epsilon_{\text{part}} \rangle$ follows a monotonic increasing trend from small to large b. Similarly, on the right side of Fig. 14, the participant eccentricity values calculated using my MCG model (blue points) are clearly in good agreement with the CMS data (purple points with error bars) [14]. These CMS-provided values are also listed in Table 4 below, which can be directly compared with the values in Table 3 of the average ϵ, S, b, and N_{part} for various centrality classes generated from my MCG simulations.

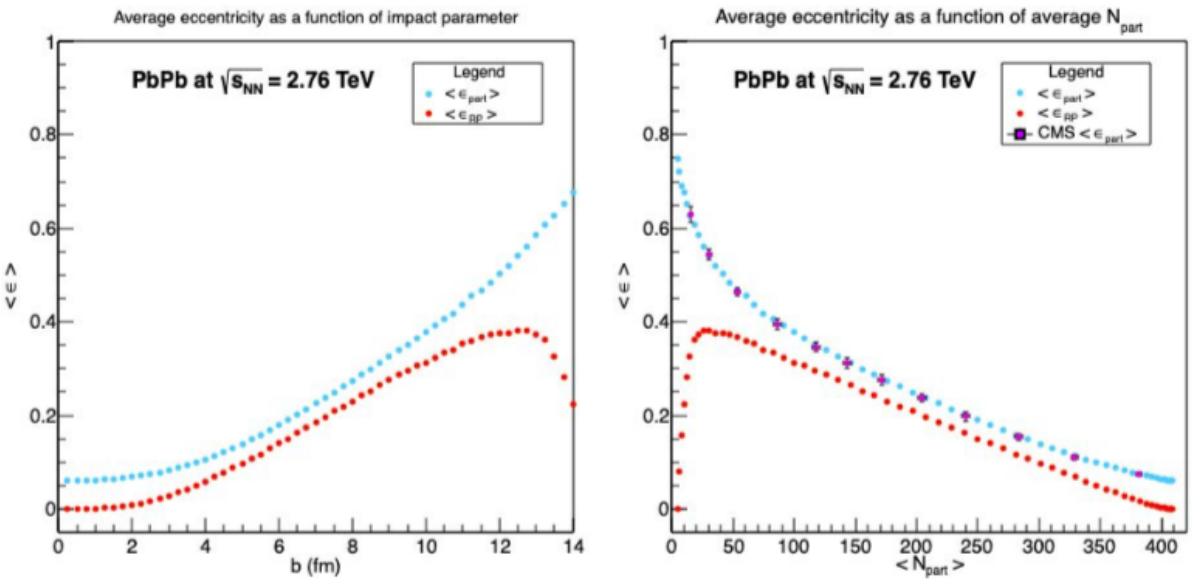

Figure 14: Average ϵ_{RP} and ϵ_{part} as a function of b (left) and average N_{part} (right) for 2.76 TeV Pb+Pb.

The average number of participants is again being slightly overestimated, as seen in Tables 3 and 4 below, but the eccentricity and overlap area values still remain fairly consistent between the data and the model, especially for more central events. As with the Au+Au case, the same general trends are observed with Pb+Pb collisions: small b events are associated with high numbers of participants, large overlap areas, and small eccentricities, while large b collisions have fewer participants, smaller overlap areas, and larger eccentricities (which means a sharper almond-shaped region that experiences greater fluctuations in orientation from event to event).

Centrality	**0-5%**	**5-10%**	**10-15%**	**15-20%**	**20-25%**	**25-30%**
ΣE_{T} (TeV)	≥ 3.25	2.55-3.25	2.025-2.55	1.6-2.025	1.25-1.6	0.95-1.25
b_{avg} (fm)	2.32	4.14	5.40	6.39	7.25	8.04
N_{part}	377	334	286	245	209	176
ϵ_{RP}	0.0170	0.0630	0.113	0.156	0.192	0.228
ϵ_{part}	0.0751	0.110	0.154	0.195	0.234	0.272
S_{RP} (fm^2)	29.12	26.71	24.1	21.76	19.67	17.71
S_{part} (fm^2)	29.07	26.63	24.0	21.64	19.52	17.54
	30-35%	**35-40%**	**40-50%**	**50-60%**	**60-70%**	**70+%**
ΣE_{T} (TeV)	0.75-0.95	0.55-0.75	0.3-0.55	0.15-0.3	0.1-0.15	<0.1
b_{avg} (fm)	8.72	9.36	10.24	11.30	12.06	14.12
N_{part}	148	124	92.7	60.5	41.4	12.6
ϵ_{RP}	0.256	0.282	0.315	0.343	0.354	0.175
ϵ_{part}	0.305	0.338	0.386	0.443	0.492	0.685
S_{RP} (fm^2)	16.06	14.51	12.41	10.02	8.35	3.67
S_{part} (fm^2)	15.85	14.28	12.12	9.64	7.87	3.38

Table 3: Calculated eccentricities and overlap areas for centrality classes based on cuts in ΣE_{T} for Pb+Pb at $\sqrt{s_{\mathrm{NN}}} = 2.76$ TeV. All reported values are averages except for the ΣE_{T} ranges that designate centrality classes.

Centrality	**0-5%**	**5-10%**	**10-15%**	**15-20%**	**20-25%**	**25-30%**
N_{part}	381±2	329±3	283±3	240±3	204±3	171±3
ϵ_{part}	0.074±0.003	0.111±0.005	0.154±0.007	0.198±0.009	0.238±0.009	0.276±0.010
S_{part} (fm^2)	29.4±1.2	26.6±1.1	24.0±1.0	21.6±1.0	19.5±0.9	17.5±0.8
	30-35%	**35-40%**	**40-50%**	**50-60%**	**60-70%**	**70-80%**
N_{part}	143±3	118±3	86.2±2.8	53.5±2.5	30.5±1.8	15.7±1.1
ϵ_{part}	0.312±0.011	0.346±0.010	0.395±0.010	0.465±0.008	0.543±0.011	0.630±0.016
S_{part} (fm^2)	15.7±0.8	14.1±0.7	12.0±0.6	9.4±0.5	7.1±0.4	4.8±0.3

Table 4: Average ϵ_{part}, S_{part}, and N_{part} with estimated uncertainties for various centrality classes of Pb+Pb collisions at $\sqrt{s_{\text{NN}}} = 2.76$ TeV, determined by the CMS Collaboration [14].

Fig. 15 below shows the correlations between ϵ_{part} and N_{part} and between S_{part} and N_{part}. There is a roughly linear positive correlation between the number of participants and the overlap area of the participants (Fig. 15 on the right), which makes sense given more participating nucleons would naturally cover a larger area. On the left of Fig. 15, there appears to be an approximately negative correlation between the participant eccentricity and the number of participants for a given nucleus-nucleus collision. More importantly, the distribution of eccentricity values becomes much broader and more diffuse for low N_{part}. In those more peripheral events, fluctuations in the positions of the nucleons from event to event have a greater impact on the resulting calculation; furthermore, that behavior demonstrates the need for Monte Carlo methods in these simulations, since only using the averages would not capture the entirety of the physics at work in these complicated processes.

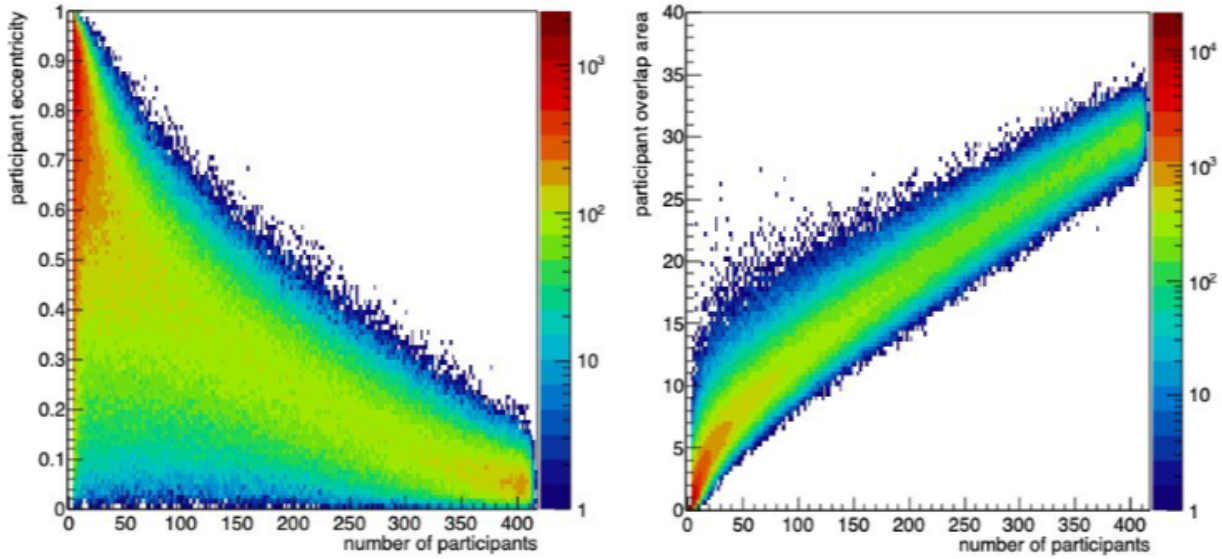

Figure 15: Correlation between the participant eccentricity and the number of participating nucleons (left), and between the participant overlap area and the number of participants (right).

5 Conclusions and future work

The Glauber model comprises a series of phenomenological techniques that reveal information about the complex, femtoscopic many-body systems that are relativistic heavy ion collisions. This methodology accomplishes this by treating nucleus-nucleus collisions as sequences of independent nucleon-nucleon interactions. The CMS and STAR experiments collide ultra-relativistic gold and lead nuclei (containing high numbers of nucleons) and collect data on the energy, momentum, and identity of the outgoing particles. The Monte Carlo version of this model incorporates random number generation to simulate these events and estimate values of the impact

parameter, number of participants, and number of nucleon-nucleon collisions based on experimental data with the help of a measured nuclear density function and inelastic nucleon-nucleon cross-section. Determining these quantities allows for better understanding of the bulk and transport properties of the hot, dense phase of matter produced in a heavy ion collision, which is thought to be a QGP. By producing and studying this exotic state of matter in experimental settings, physicists seek to improve our collective understanding of QCD-governed matter and the state of the universe in its first few microseconds of existence.

A basic Monte Carlo Glauber model estimates b, N_{part}, and N_{coll} as functions of centrality using experimental transverse energy and multiplicity data. Additional calculations can be added to the model to quantify geometric quantities like the overlap area of the nucleus-nucleus collision and the eccentricity of this almond-shaped overlap. The importance of knowing these quantities, especially the eccentricity, comes from their relevance to elliptic flow analysis. The eccentricity characterizes the initial spatial anisotropy, which is responsible for the final anisotropy in the momentum distribution for the emitted charged particles. The transfer of anisotropy is studied as part of the collective flow of quarks and gluons observed in the dense medium produced in relativistic heavy ion collisions. Such a strong anisotropic collective flow of particles constitutes a key piece of evidence for the formation of a hot, dense state of strongly interacting matter, i.e. a strongly-coupled QGP. Elliptic flow is quantified using correlations in azimuthal angle between produced hadrons, where its strength is given by v_2, the second term in a Fourier expansion of the particles' invariant yield—the integrated flow of produced particles over a wide range in rapidity and transverse momentum [14]. Eccentricity calculations are useful for characterizing collision shapes across various event classes and for $v_2/\epsilon_{\text{part}}$ analysis. Additionally, the eccentricity is relevant to measurements of elliptic flow of heavy mesons, which is of interest since it has not yet been determined if heavy quarks undergo the same type of hydrodynamic flow as light quarks. In either case, elliptic flow preserves the anisotropy of the collision in its early state and therefore can reveal information about this stage in the evolution of a heavy ion collision.

Future work on this particular project would involve the analysis of more datasets to provide more values of ϵ for elliptic flow analysis—beyond comparisons of this model with published results that were determined using the same techniques. This phenomenon of elliptic flow is a crucial pillar of evidence for the formation of a Quark-Gluon Plasma in experimental settings. Creating a QGP requires collisions between heavy ions moving at nearly the speed of light in order to reach the extreme temperature and density conditions seen in the very early universe. Continued study of the complex, high-multiplicity nucleus-nucleus collisions occurring at the LHC and RHIC will provide further insights into the behavior of quantum chromodynamics and nuclear matter at high energies, where the constituent particles are color-deconfined and quasi-free, and into the state of matter in the very early universe.

Acknowledgements

Thank you to Professor Calderón for his invaluable guidance and support throughout this project, to the other members of the Nuclear Physics Group for their assistance, to Professors Zieve, Curro, and Cebra for organizing the REU program, and to UC Davis and the National Science Foundation for providing me with the space and resources to complete this research.

References

[1] M. Riordan and W. Zajc, "The first few microseconds", *Scientific American* (May, 2006) 34-41, https://www.scientificamerican.com/article/the-first-few-microsecond-2006-05/.

[2] A. R. Kesich, "Upsilon Production and Suppression as Measured by STAR in $p+p$, $d+$Au, and Au + Au Collisions at $\sqrt{s_{\rm NN}} = 200$ GeV", UC Davis Ph.D Thesis (2014).

[3] R. Kunzig, "The Glue That Holds the World Together", *Discover* (Jul., 2000) 51-55, https://discovermagazine.com/2000/jul/featgluons.

[4] B. Jacak and P. Steinberg, "Creating the perfect liquid in heavy-ion collisions", *Physics Today* **63** no. 5 (2010), https://doi.org/10.1063/1.3431330.

[5] CMS Collaboration, "Measurement of nuclear modification factors $\Upsilon(1S)$, $\Upsilon(2S)$, and $\Upsilon(3S)$ mesons in PbPb collisions at $\sqrt{s_{\rm NN}} = 5.02$ TeV", *Physics Letters B* **790** (Mar., 2019) 270-293, https://doi.org/10.1016/j.physletb.2019.01.006.

[6] CERN, "Heavy ions and quark-gluon plasma", https://home.cern/science/physics/heavy-ions-and-quark-gluon-plasma.

[7] National Research Council, "Chapter 4: Matter at Extreme Densities" in *Nuclear Physics: The Core of Matter, The Fuel of Stars* (1999), Washington, DC: The National Academies Press. https://doi.org/10.17226/6288.

[8] M. Anderson *et al.*, "The STAR Time Projection Chamber: A Unique Tool for Studying High Multiplicity Events at RHIC", *Nuclear Instruments and Methods in Physics Research Section A* **499** no. 2-3 (Mar., 2003) 659-678, https://doi.org/10.1016/S0168-9002(02)01964-2.

[9] M. L. Miller, K. Reygers, S. J. Sanders, and P. Steinberg, "Glauber Modeling in High-Energy Nuclear Collisions", *Annual Review of Nuclear and Particle Science* **57** (May, 2007) 205-243, https://www.annualreviews.org/doi/pdf/10.1146/annurev.nucl.57.090506.123020.

[10] M. Calderón de la Barca Sánchez. *Glauber Model + Particle Production Model.* Summer Research Program. Lecture conducted at the University of California - Davis (2017).

[11] CMS Collaboration, "Dependence on pseudorapidity and on centrality of charged hadron production in PbPb collisions at $\sqrt{s_{\rm NN}} = 2.76$ TeV", *Journal of High Energy Physics* (Oct., 2011), https://arxiv.org/pdf/1107.4800.

[12] T. Hirano and Y. Nara, "Eccentricity fluctuation effects on elliptic flow in relativistic heavy ion collisions", *Physical Review* **C79** (2009) 064904, https://journals.aps.org/prc/abstract/10.1103/PhysRevC.79.064904.

[13] M. Miller and R. Snellings, "Eccentricity fluctuations and its possible effect on elliptic flow measurements" (Dec., 2003), https://arxiv.org/abs/nucl-ex/0312008.

[14] CMS Collaboration, "Measurement of the elliptic anisotropy of charged particles in PbPb collisions at $\sqrt{s_{\rm NN}} = 2.76$ TeV", *Physical Review C* (Jan., 2013), https://arxiv.org/pdf/1204.1409.